ARCHIVE OF MECHANICAL ENGINEERING

DOI: 10.24425/ame.2025.153737 2025, Vol. 72, No. 1, pp. 31–55

Nhu Thanh VO [1], Anh-Duc PHAM [1], Dac Minh Triet NGUYEN[1]

Hierarchical sliding mode control with oscillation compensation for low-cost inverted pendulum systems using hardware-in-loop

Received 2 November 2024, **Revised** 13 February 2025, **Accepted** 16 February 2025, **Published online** 1 March 2025

Keywords: hierarchical sliding mode control (HSMC), nonlinear control, inverted pendulum, hardware-in-the-loop, unwanted oscillation

This research presents three major contributions to the nonlinear control of underactuated systems. First, the identification and characterization of a 2.5 Hz oscillatory phenomenon in the low-cost inverted pendulum system, addressing challenges from mechanical elasticity and electrical delays, is reported. Second, the Hierarchical Sliding Mode Control (HSMC) framework is developed to control this underactuated system considering its unwanted oscillatory phenomenon. This HSMC control system is used to achieve superior disturbance rejection, maintaining cart position within ±0.05 m compared to PD-LQR's ±0.35 m under pure oscillatory disturbances, while reducing energy consumption by 32%. Third, a comprehensive Hardware-in-the-Loop (HIL) implementation using the F28379D microcontroller, which provides real-time parameter adjustment capabilities, is established. The stability of the system is theoretically validated through Lyapunov analysis and homoclinic orbit characterization. Experimental results demonstrate the effectiveness of the HSMC controller in maintaining pendulum angular oscillations within ±2.5°, significantly outperforming PD-LQR's ±5° range under combined disturbances.

1. Introduction

Most real-world systems exhibit inherent nonlinear behavior, deviating from the principles of superposition and homogeneity that govern linear systems. This nonlinearity often arises due to the presence of components with nonlinear characteristics, such as viscous and frictional forces, harmonic signal components, and

✉ Anh-Duc PHAM, e-mail: ducpham@dut.udn.vn

[1]Faculty of Mechanical Engineering, The University of Danang – University of Science and Technology, Danang, Vietnam

abrupt disturbances [1, 2]. These nonlinear elements introduce significant complexities that challenge the accurate modeling, analysis, and effective control of such systems [3]. Despite these challenges, conventional linear control techniques, including PID, LQR, and LQG controllers, are still widely employed in control design for nonlinear systems [4–7]. The PD-LQR controller, extensively studied in the context of the inverted pendulum, has proven effective in balancing control and energy efficiency in underactuated systems [8, 9]. However, this approach is accompanied by drawbacks, including the limitation of control only at equilibrium or fixed operating points, and the necessity to eliminate or linearize the nonlinear components to generate a simplified, linear model. Consequently, the control signals derived from these linear controllers may not be well-suited or optimally effective when applied to inherently nonlinear real-world systems.

To address these limitations, researchers in the field of control theory have been actively exploring nonlinear control techniques as a more effective solution to address the inherent complexities of nonlinear systems. Nonlinear systems are commonly characterized by nonlinear equations, which pose greater analytical and computational challenges compared to linear equations [10]. Analyzing the behavior of nonlinear systems often necessitates the use of numerical or approximate methods. Unlike their linear counterparts, nonlinear systems can display intricate phenomena such as bifurcations, chaos, and limit cycles, adding a layer of complexity not observed in linear systems. Recent studies in the field of mechanical actuator control have explored various nonlinear controllers [3, 11, 12, 14]. For instance, a Lyapunov-based approach has been used to develop an improved control law based on feedback linearization, considering variations in supply pressure in an electrohydraulic system [11]. The adaptive component of the controller is employed to offset deviations in system characteristics from the predominant linear model, aiming to enhance performance in the servo-mechanical system [12]. Additionally, a neural network controller has also been used to handle nonlinear factors and improve the control performance of a 2-axis pneumatic artificial muscle manipulator [13]. Moreover, a fuzzy-adaptive controller has been utilized to address uncertainties and enhance the dynamic response of the rotary inverted pendulum system, showcasing its effectiveness in solving the nonlinearities and disturbances inherent in underactuated setups [14]. Sliding mode control techniques have also emerged as a promising approach for addressing the challenges posed by nonlinear systems, particularly for underactuated systems.

Designing control laws that provide the desired performance to closed-loop systems in the presence of disturbances and uncertainties is a challenging task for control engineers [15, 16]. This has led to significant interest in the development of robust control methods, such as sliding mode control, to address this problem. Sliding mode control (SMC) is a well-established technique that has gained widespread attention due to its inherent robustness to parameter variations and external disturbances [17, 18]. While the conventional sliding mode control approach offers superior robustness, it is not without its drawbacks, as it is susceptible to the

chattering phenomenon, which can lead to undesirable high-frequency oscillations in the control input. These oscillations may compromise system stability and degrade overall performance [19–21]. To address this issue, researchers have explored various modifications and enhancements to the SMC framework, such as dynamic sliding mode control and backstepping-based approaches [21, 22]. These advanced techniques combine the robust characteristics of sliding mode control with strategies aimed at mitigating the chattering problem, resulting in a more comprehensive and effective control solution for nonlinear systems. These improvements allow the system to handle a wider range of uncertainties and disturbances while maintaining stability and performance [23–25].

When implementing low-cost experimental systems, several issues arise, particularly related to unknown unstable factors, which have been confirmed in previous studies [26]. These systems often exhibit unexpected behaviors, such as vibrations caused by the elasticity of components like rubber belt transmissions. In such cases, the elasticity introduces additional dynamic delays and oscillations, which can negatively impact control performance. Moreover, electrical equipment used in low-cost setups can contribute to delay factors, further complicating the system's dynamics. In this context, the integration of hardware-in-the-loop (HIL) systems plays a crucial role [27]. HIL allows real-time interaction between the Matlab environment and the physical system, enabling the manual adjustment of system parameters and responses during operation. This capability provides a valuable platform for refining control strategies by simulating real-world disturbances and fine-tuning the system's behavior in real-time.

This paper presents a Hardware-in-Loop Implementation of HSMC for Low-Cost Nonlinear Systems considering Unwanted Oscillation. First, the dynamics model of a low-cost nonlinear system based on the model of the inverted pendulum is introduced. The identification and characterization of a 2.5 Hz oscillatory phenomenon in this low-cost system, addressing challenges from mechanical elasticity and electrical delays, is reported. Second, the Hierarchical Sliding Mode Control (HSMC) framework is developed to control this underactuated system considering its unwanted oscillatory phenomenon. The stability of the system is theoretically validated through Lyapunov analysis and homoclinic orbit characterization. More importantly, an experimental model is constructed to assess the method's effectiveness, utilizing the F28379D microcontroller board with code compiled in the DSP C2000 toolbox package of the Simulink environment. The proposed system incorporates HIL implementation with real-time parameter adjustment to simulate nonlinear dynamics while accounting for unwanted oscillation factors, such as those arising from the elasticity of mechanical components and delays in electrical equipment. Simulations incorporating these disturbances yield results that closely resemble the behavior observed in real-world experiments. The similarity between the simulation results and experimental data validates the effectiveness of the proposed control strategy in handling both expected and unexpected oscillatory behaviors in low-cost nonlinear systems.

2. Mathematical model

The model of the inverted pendulum system moved by a cart is described in the $Oxyz$ coordinate system, as shown in Fig. 1. The system consists of a pendulum characterized by mass m_{pen}, l_{pen} represents the distance from the pivot point on the cart to the center of the pendulum rod, and length $2l_{\text{pen}}$ attached to a moving cart with mass m_{cart}. While the cart moves back and forth along the y-axis under the influence of a pushing force F_{cart}, the pendulum swings at an angle θ around a pivot point on the cart and is affected by gravitational acceleration g. During operation, the performance of the system can also be influenced by factors such as the inertia moment at the center of the pendulum J_{pen}, the friction of the pendulum at the pivot f_{pen}, and the friction of cart f_{cart}. Table 1 shows the parameters of the inverted pendulum system. Additionally, the dynamic model of the pendulum is a system with two degrees of freedom and can be analyzed in the Oyz reference frame. The state variables of the inverted pendulum system are defined as: y represents the real position of the cart along the y-axis in the Oyz reference frame, and θ denotes the angle of the pendulum relative to the vertical axis. $\dot{y}$ and $\dot{\theta}$ represent the derivative of y and θ (*also known as the velocity of the cart and the pendulum*), respectively.

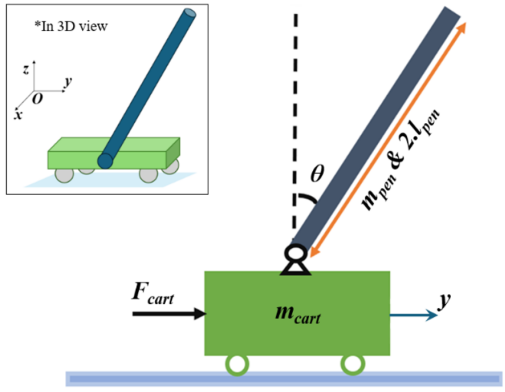

Fig. 1. Free-body diagram of the pendulum-on-cart system

Table 1. Parameters of the inverted pendulum system

Component	Parameter	Symbol (unit)	Value
Pendulum	Mass	m_{pen} (kg)	0.2
	Length	l_{pen} (m)	0.3
	Inertial moment	J_{pen} (kg m^2)	0.006
	Friction	f_{pen} (N m s)	0.005
Cart	Mass	m_{cart} (kg)	0.5
	Maximum cart travel	l_{cart} (m)	0.42
	Friction	f_{cart} (N m s)	0.1

The equation of motion of the pendulum-on-cart is written in Eq. (1):

$$\begin{aligned}(m_{\text{cart}} + m_{\text{pen}})\ddot{y} + m_{\text{pen}} l_{\text{pen}} \left(\ddot{\theta}\cos\theta - \dot{\theta}^2 \sin\theta\right) &= F_{\text{cart}} - f_{\text{cart}}\dot{y}\,,\\ (J_{\text{pen}} + m_{\text{pen}} l_{\text{pen}}^2)\ddot{\theta} + m_{\text{pen}} l_{\text{pen}} \left(\ddot{y}\cos\theta - g\sin\theta\right) &= -f_{\text{pen}}\dot{\theta}\,.\end{aligned} \tag{1}$$

Choosing the state variables $X = (x_1, x_2, x_3, x_4)$ for input variables $\left(y, \dot{y}, \theta, \dot{\theta}\right)$, respectively.

$$\begin{aligned}\dot{x}_1 &= x_2\,,\\ \dot{x}_2 &= f_1(X) + b_1(X)F_{\text{cart}}\,,\\ \dot{x}_3 &= x_4\,,\\ \dot{x}_4 &= f_2(X) + b_2(X)F_{\text{cart}}\,,\end{aligned} \tag{2}$$

where:

$$\begin{aligned}f_1 &= \Delta^{-1}\begin{pmatrix}(m_{\text{pen}} l_{\text{pen}}^2 + J_{\text{pen}})(m_{\text{pen}} l_{\text{pen}}\dot{\theta}^2 \sin(\theta) - f_{\text{pen}}\dot{y})\\ + m_{\text{pen}} l_{\text{pen}} f_{\text{cart}}\dot{\theta}\cos(\theta) - m_{\text{pen}}^2 l_{\text{pen}}^2 g\cos(\theta)\sin(\theta)\end{pmatrix};\\ b_1 &= \Delta^{-1}\left(m_{\text{pen}} l_{\text{pen}}^2 + 1\right);\\ f_2 &= \Delta^{-1}\begin{pmatrix}-(m_{\text{cart}} + m_{\text{pen}}) f_{\text{cart}}\dot{\theta} + m_{\text{pen}} g l_{\text{pen}}\sin(\theta)(m_{\text{cart}} + m_{\text{pen}})\\ + m_{\text{pen}} l_{\text{pen}} f_{\text{pen}}\dot{y}\cos(\theta) - m_{\text{pen}}^2 l_{\text{pen}}^2\dot{\theta}^2\cos(\theta)\sin(\theta)\end{pmatrix};\\ b_2 &= \Delta^{-1}\left(m_{\text{pen}} l_{\text{pen}}\cos(\theta)\right);\\ \Delta &= (m_{\text{cart}} + m_{\text{pen}})(J_{\text{pen}} + m_{\text{pen}} l_{\text{pen}}^2) - m_{\text{pen}}^2 l_{\text{pen}}^2\cos(\theta).\end{aligned}$$

The key challenge with this inverted pendulum system is the need to maintain stable upright control of the pendulum throughout the system's motion, using a motor attached to the wheels of the cart. Thus, this inverted pendulum is a typical model of underactuated model and exhibits significant nonlinear characteristics during its operation. This may be due to the natural oscillation frequency of the system changing over time [10] or may be affected by undesirable vibrations resulting from the system's own structural characteristics [26]. In this paper, the nonlinear characteristics of the low-cost pendulum-on-cart model according to the various of the input value will be introduced in the next section. Therefore, a robust control structure based on the HSMC method is essential to achieve stable balancing control when the pendulum is raised upright.

3. Design of HSMC system

The structure of HSMC is shown in Fig. 2. Overall, the control system consists of two major sliding surfaces S_{x1} and S_{x2}. The first sliding surfaceS_{x1} (coincides with s_{x1}) is formulated based on the error of the cart positione_{x1} and the error of the cart velocity $\dot{e}_{x1}$. It is responsible for controlling the position of the cart converging

to zero. The second sliding surface S_{x2} is also structured by sliding surface S_{x1} and sub-sliding surface s_{x2} which is formed by the error of the pendulum's angle e_{x1} and pendulum's rotational velocity $\dot{e}_{x2}$. This surface is tasked with maintaining stability in all state variables of the system, and its control law significantly influences the system.

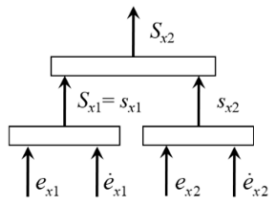

(a) Structure of sliding surfaces for HSMC

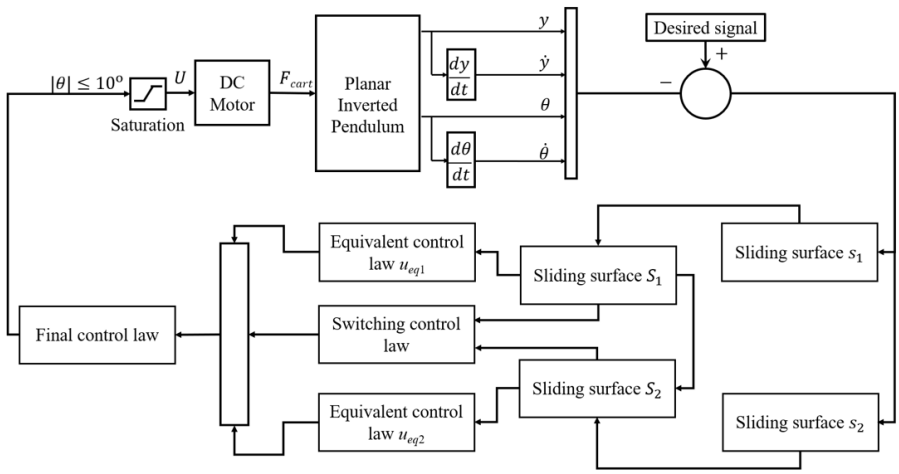

(b) Control system of the inverted pendulum with HSMC

Fig. 2. Structure of the HSMC approach to control the balance of the inverted pendulum

The HSMC is designed to control the inverted pendulum system considering its nonlinear characteristics and effects of unwanted oscillations as the following:

- Step 1: Choosing the sub-sliding surfaces s_{x1} and s_{x2}

$$\begin{aligned} s_{x1} &= c_{x1} e_{x1} + \dot{e}_{x1}\,, \\ s_{x2} &= c_{x2} e_{x2} + \dot{e}_{x2}\,, \end{aligned} \tag{3}$$

with: c_{x1}, c_{x2} (positive constant): coefficients for errors of cart position and pendulum angle, respectively. e_{x1}, e_{x2} is the error of the cart position and pendulum angle, respectively.

$$\begin{aligned} e_{x1} &= y - y_d\,, \\ e_{x2} &= \theta - \theta_d \end{aligned}$$

in that, y and θ are the real cart position and pendulum angle; y_d, θ_d for the desired cart position and pendulum angle.
Due to the balance point of the system at the original point, the desired cart position and pendulum angle should become zero ($y_d = 0$, $\theta_d = 0$).
Thus, the Eq. (3) can be written as the following:

$$\begin{aligned} s_{x1} &= c_{x1} y + \dot{y}\,, \\ s_{x2} &= c_{x2} \theta + \dot{\theta}. \end{aligned} \tag{4}$$

- Step 2: The control law for the first sliding surface S_{x1} is designed.
The sliding surface S_{x1} is used to control the position and velocity of the cart. Thus, the configuration of S_{x1} and its derivative $\dot{S}_{x1}$ is introduced:

$$S_{x1} = s_{x1} = c_{x1} y + \dot{y}\,, \tag{5}$$

$$\dot{S}_{x1} = c_{x1}\dot{y} + \ddot{y} = c_{x1}\dot{y} + \left(f_1(X) + b_1(X) u_{eq1}\right) \tag{6}$$

with the control law for this surface:

$$u_1 = u_{eq1} + u_{sw1}\,,$$

where, u_{eq1} and u_{sw1} are the equivalent control law and switching control law of the first surface, respectively. While as, u_{sw1} is selected as in Eq. (7), u_{eq1} is determined by giving $\dot{S}_{x1}$ to zero.

$$u_{eq1} = -b_1^{-1}(X)\left(c_1\dot{y} + f_1(X)\right), \tag{7}$$

$$u_{sw1} = -b_1^{-1}(X)\left(k_1 S_{x1} + \eta_1 \mathrm{sign}(S_{x1})\right), \tag{8}$$

$$u_1 = -b_1^{-1}(X)\left(c_1\dot{y} + f_1(X) + k_1 S_{x1} + \eta_1 \mathrm{sign}(S_{x1})\right). \tag{9}$$

- Step 3: Proving the stability of the system which is represented by the cart position.
First of all, the Lyapunov function for the first sliding surfaces and its derivative following the time are determined based on Eqs. (5)–(9):

$$V_1 = \frac{1}{2} S_{x1}^2\,, \tag{10}$$

$$\dot{V}_1 = S_{x1}\dot{S}_{x1} = S_{x1}\left(-k_1 S_{x1} - \eta_1 \mathrm{sign}(S_{x1})\right) = -k_1 S_{x1}^2 - \eta_1 \left|S_{x1}\right|, \tag{11}$$

where,

$$\begin{aligned} S_{x1} &= s_{x1} = c_{x1} y + \dot{y}, \\ \dot{S}_{x1} &= c_{x1}\dot{y} + \ddot{y} \\ &= c_{x1}\dot{y} + \left(f_1(X) + b_1(X)\left[-b_1^{-1}(X)\left(c_1\dot{y} + f_1(X) + k_1 S_{x1} + \eta_1 \mathrm{sign}(S_{x1})\right)\right]\right) \\ &= -k_1 S_{x1} - \eta_1 \mathrm{sign}(S_{x1}). \end{aligned}$$

Therefore, based on Eqs. (10) and (11), the derivative of V_1 will become:

$$\dot{V}_1 = -2k_1V_1 - \eta_1\sqrt{2}V_1^{0.5} \leqslant -\eta_1\sqrt{2}V_1^{0.5}\,. \tag{12}$$

Based on the Lemma for proving the asymptotic stability proof and finite-time convergence [28–30], the system is asymptotically stable (V_1 converges to zero). Therefore, the sliding surface S_{x1} converges to the origin in finite time. This results in the cart position to zero.

- Step 4: The control law for the second sliding surface S_{x2} is designed. The second sliding surface S_{x2} is encompassed by all state variables.

$$S_{x2} = \alpha S_{x1} + s_{x2} \quad \text{(the coefficient } \alpha \text{ is a positive constant)} \tag{13}$$

with the control law for the second major sliding surface is formulated as:

$$u_2 = u_{eq1} + u_{eq2} + u_{sw2}\,, \tag{14}$$

where, u_{eq2} and u_{sw2} are the equivalent control law and switching control law of the second surface, respectively.

$$u_{eq2} = -b_2^{-1}(X)\left(c_2\theta + f_2(X)\right),$$
$$u_{sw2} = -\frac{\alpha b_1(X)u_{eq2} + b_2(X)u_{eq1} + k_2S_{x2} + \eta_2\text{sign}(S_{x2})}{\alpha b_1(X) + b_2(X)}\,.$$

Thus:

$$u_2 = \frac{\alpha b_1(X)u_{eq1} + b_2(X)u_{eq2} - k_2S_{x2} - \eta_2\text{sign}(S_{x2}))}{\alpha b_1(X) + b_2(X)}\,. \tag{15}$$

- Step 5: Proving the stability of the whole system. The Lyapunov function for the first sliding surfaces and its derivative following the time are determined:

$$V_2 = \frac{1}{2}S_{x2}^2\,, \tag{16}$$
$$\dot{V}_2 = S_{x2}\dot{S}_{x2} = -k_2S_{x2}^2 - \eta_2S_{x2}\text{sign}(S_{x2}) \leqslant -k_2S_{x2}^2 - \eta_2\left|S_{x2}\right|, \tag{17}$$

where,

$$\begin{aligned}
S_{x2} &= \alpha\left(c_1x_1 + x_2\right) + \left(c_2x_3 + x_4\right),\\
\dot{S}_{x2} &= \alpha\left(c_1\dot{x}_1 + \dot{x}_2\right) + \left(c_2\dot{x}_3 + \dot{x}_4\right)\\
&= \alpha\left(-b_1u_{eq1}\right) + \left(-b_2u_{eq2}\right)\\
&\quad + \left(\alpha b_1 + b_2\right)\frac{\alpha b_1(X)u_{eq1} + b_2(X)u_{eq2} - k_2S_{x2} - \eta_2\text{sign}(S_{x2})}{\alpha b_1(X) + b_2(X)}\\
&= -k_2S_{x2} - \eta_2\text{sign}(S_{x2}).
\end{aligned}$$

Therefore, based on Eqs. (16) and (17), the derivative of V_1 will become:

$$\dot{V}_2 = -2k_2V_2 - \eta_2\sqrt{2}V_2^{0.5} \leqslant -\eta_2\sqrt{2}V_2^{0.5}\,. \tag{18}$$

Thus, similar to S_{x1}, S_{x2} converges to the origin in finite time and the pendulum is stable.

4. Experimental model

The experimental inverted pendulum system is shown in Fig. 3 with its parameters presented in Table 1. A frame holds the entire system in place. Through a coupling, a uniform rod is fastened to the cart. The motor's responsibility is to move the cart, which is powered by a belt, so that the rod stays stable. The cart's maximum travel distance is limited to a distance of 0.42 m. To detect the angular position of the rod, the first encoder sensor is attached to the rod's pivot. To measure the sliding cart's displacement and speed, a second angle sensor is mounted on the other side of the engine. Fig. 4 depicts the electrical connection diagram for the inverted pendulum system. The DC motor operates with a rated voltage of 24 V. The H-bridge circuit used is the Hbr-H 250 W – 15 A. Subsequently, the 5 V power supply is regulated through an LM2596 voltage regulator from the 24 V source to sustain the operation of the central C2000 control circuit, as well as the angle and position sensors. Signals from these sensors are feedback to the C2000 control unit. The central control unit then calculates control values and outputs PWM signals to regulate the motor through the H-bridge. The model executes both the PD-LQR and HSMC algorithms, with the comparison results presented in the following sections. The PD-LQR controller employs a proportional-derivative (PD) control law, where *Kp* is the proportional gain and *Kd* is the derivative gain. The LQR minimizes the cost function with Q and R as weighting matrices. While the LQR gains are fixed because the K gains are precomputed and remain constant, PD gains

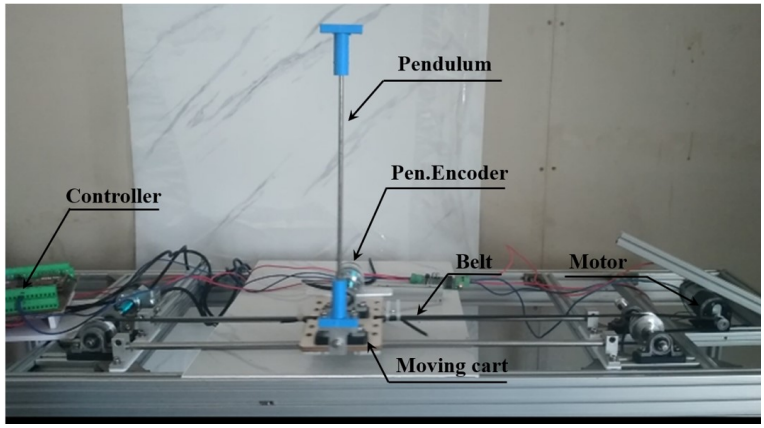

Fig. 3. Experimental setup of the inverted pendulum system

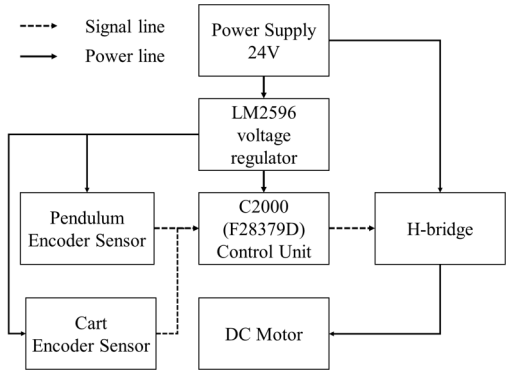

Fig. 4. Actuator, sensor, and control system

are manually tuned. For HSMC, the sliding surface parameters c_{x1} and c_{x2} can be adjusted. Both controllers are fine-tuned to achieve the best possible performance.

Fig. 5 illustrates the hardware-in-loop setup for the inverted pendulum, transitioning from Simulink to the F28379D hardware. Initially, the peripherals are configured, comprising the Enhanced Pulse Width Modulation (ePWM) block responsible for generating varying voltages to control the DC motor through an H-bridge. The Enhanced Quadrature Encoder Pulse (eQEP) blocks are utilized in conjunction with a linear or rotary incremental encoder to gather position, direction, and speed information from both the pendulum and cart. GPIO blocks are employed to manage the direction of the DC motor through the H-bridge, and the SCI transmit block is engaged to send scalar or vector data using the specified SCI USB. Following this, a Simulink block containing Matlab code is employed

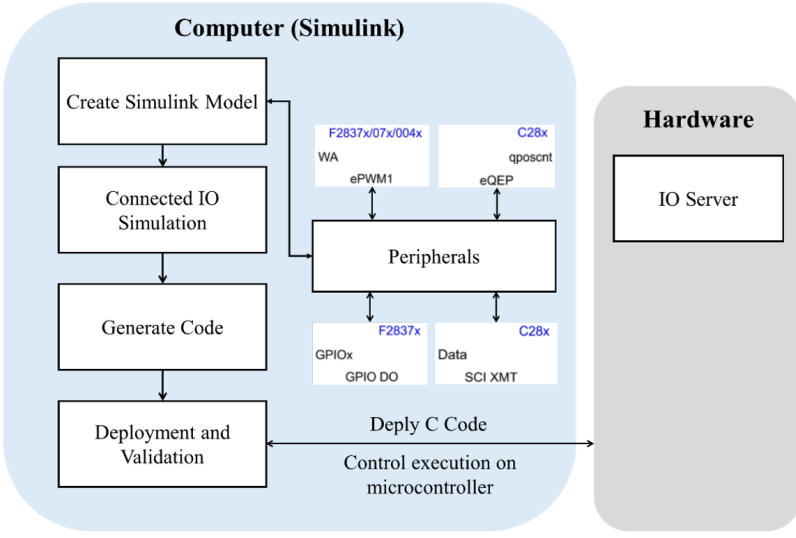

Fig. 5. The hardware-in-loop setup for the inverted pendulum

to manage the code for the HSMC and PD-LQR algorithm. Subsequently, these blocks are interlinked, forming a comprehensive code structure for the system. Ultimately, the experimental system is implemented after generating the code using Matlab/Simulink.

5. Results and discussion

5.1. Oscillation analysis and system response

The experimental analysis reveals oscillatory behavior in the inverted pendulum under varying conditions. This behavior is influenced by cart displacement, velocity, and the initial release angle, as shown in Fig. 6. The time-domain data

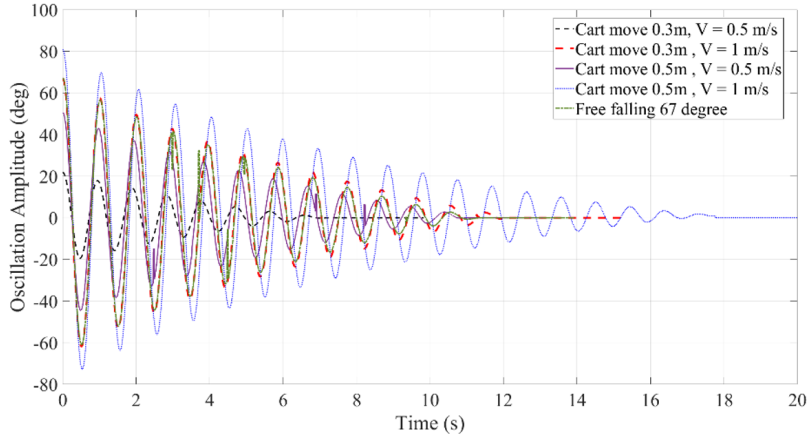

(a) Time-domain analysis

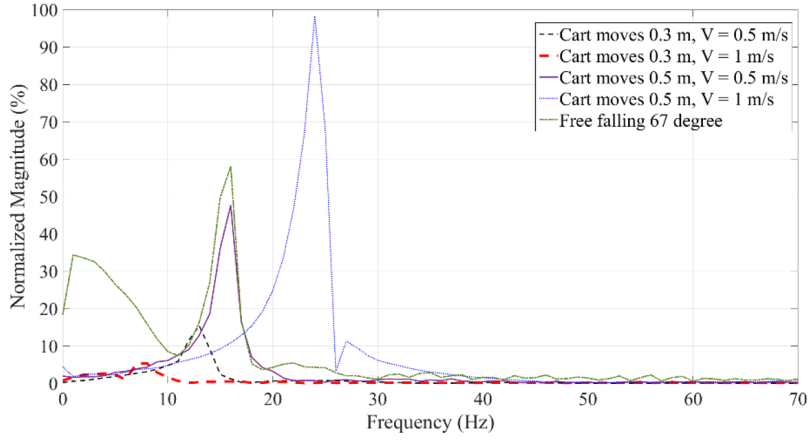

(b) Frequency-domain analysis

Fig. 6. Oscillation signal and frequency of inverted pendulum under various conditions

illustrate that oscillation amplitude is directly correlated with both the cart's displacement and speed; for instance, larger displacements and higher velocities, such as the 0.5 m displacement at 1 m/s, produce more pronounced oscillations than lower-energy scenarios, exemplified by the 0.3 m displacement at 0.5 m/s. In the frequency domain, each condition exhibits unique resonant peaks, with notable frequency components around 10 Hz and 20 Hz for controlled scenarios. In contrast, the free-fall condition, where the pendulum is released from a 67° angle, introduces a distinctive low-frequency oscillation near 2.5 Hz. This unwanted oscillation likely arises from the nonlinear dynamics of the system when released from a high angle, where gravitational forces and angular momentum generate complex, uncontrolled motion. The persistence of this 2.5 Hz component, absent in other scenarios, highlights a critical system instability associated with unregulated, high-energy states. This behavior underscores the importance of control mechanisms in mitigating oscillatory instabilities in nonlinear systems like the inverted pendulum. The presence of such low-frequency oscillations in free-fall conditions suggests that advanced nonlinear control techniques, such as feedback linearization or adaptive control, may be essential for stabilizing the system and suppressing chaotic responses, especially when operating outside conventional control limits.

Fig. 7 illustrates the simulation results for the inverted pendulum system. The starting point of the simulation is when the pendulum angle is at 10° offset from the equilibrium position. Since the system is under unwanted oscillation, a harmonic input signal is added with an amplitude of 0.1 m, frequency of 2.5 Hz, and step size of 0.2 seconds acting as the nonlinear uninvited oscillation to investigate the simulation response of the system.

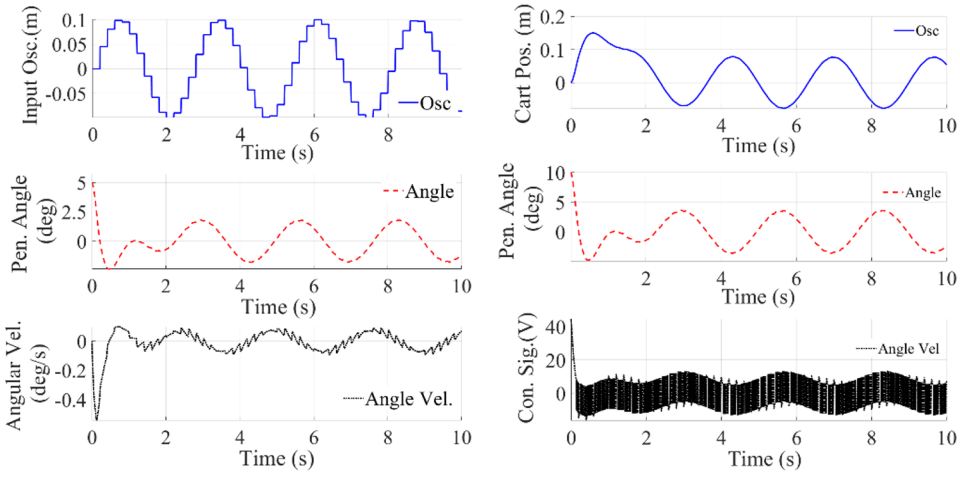

(a) Cart (b) Pendulum

Fig. 7. Cart and Pendulum response under input oscillation with 10° angle offset

5.2. Simulation results with disturbances

The simulation results presented in Fig. 8 demonstrate the dynamic behavior of the inverted pendulum system under four distinct disturbance conditions. The HSMC controller's performance was evaluated through systematic testing, including baseline operation (no disturbances), pure oscillatory disturbance, pulse disturbance, and combined oscillatory and pulse disturbance scenarios. Pulse disturbance is applied to the pendulum at the 10th second (after the swing-up phase and reaching steady state) with an amplitude of -10° to simulate unwanted nonlinear disturbance behavior in the simulation model. The response characteristics are displayed through four key state variables: cart position (m), pendulum angle ($^\circ$), cart velocity (m/s), and pendulum angular velocity ($^\circ$/s) over a 10 second simulation period, demonstrating the HSMC method's capability in disturbance rejection and stability maintenance.

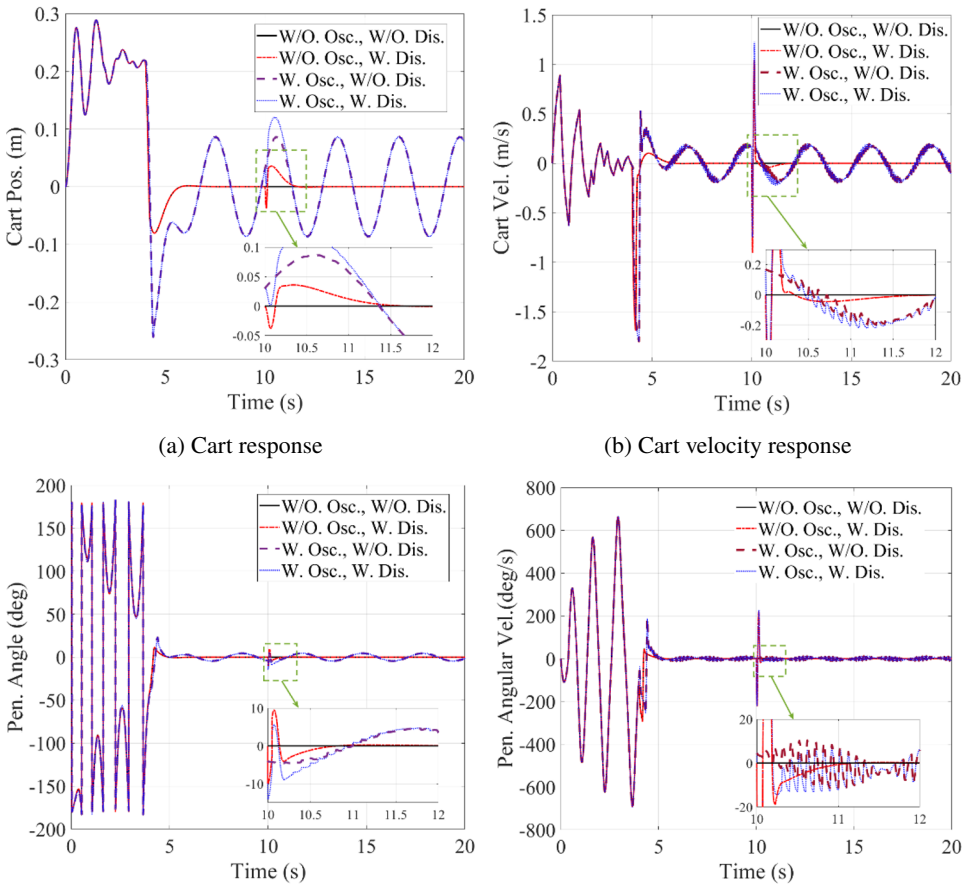

(a) Cart response

(b) Cart velocity response

(c) Pendulum response

(d) Pendulum angular velocity response

Fig. 8. System response under various disturbance conditions

Case 1: No Oscillation, No Disturbance

In this baseline scenario, without oscillation or pulse disturbance, the cart and pendulum achieve stable responses quickly. The cart position reaches a maximum deviation of approximately 0.2 m at around $t = 2$ s before stabilizing near zero. The pendulum angle exhibits a peak overshoot of 150° initially, which then stabilizes close to 0° after about 5 s. The cart and pendulum angular velocities, similarly, show initial fluctuations but settle within a few seconds, with minimal oscillations indicating successful stabilization by the HSMC control.

Case 2: No Oscillation, With Pulse Disturbance

When a pulse disturbance is introduced, the response exhibits a notable transient deviation compared to the baseline. The cart position, after initial stabilization, briefly deviates by approximately 0.1 m around 10 s due to the pulse but returns to zero, demonstrating the HSMC's robustness against transient disturbances. The pendulum angle similarly experiences a momentary shift around 10 s but returns to 0°, indicating effective disturbance rejection. Both cart and pendulum angular velocities show minor peaks corresponding to the pulse disturbance but rapidly stabilize, underscoring the HSMC's resilience in damping the transient effects.

Case 3: With Oscillation, No Pulse Disturbance

In the presence of oscillation disturbance alone, the system shows periodic fluctuations, particularly in the cart's position and velocity responses. The cart position oscillates slightly more than in the baseline case, with oscillations peaking around 0.1 m. The pendulum angle stabilizes after initial oscillations but retains small periodic deviations due to the persistent oscillation disturbance. Similarly, both cart velocity and pendulum angular velocity exhibit sustained oscillatory behavior, with the angular velocity of the pendulum reaching peaks around 100°/s periodically. This behavior indicates that while the HSMC manages the oscillations, it does not entirely eliminate their influence.

Case 4: With Both Oscillation and Pulse Disturbance

Under combined oscillation and pulse disturbances, the system faces the most challenging environment. The cart position shows significant deviations, with a peak of 0.3 m around $t = 10$ s during the pulse disturbance and continued oscillations afterward. The pendulum angle response shows marked fluctuations, momentarily exceeding 150° in the initial response and demonstrating oscillatory behavior superimposed on transient deviations from the pulse. Both cart and pendulum angular velocities reflect these compounded disturbances, with angular velocities reaching peaks up to 200°/s during the pulse and oscillating thereafter. This case highlights the limitations of the HSMC in fully neutralizing combined disturbances, though it still achieves eventual stabilization.

The HSMC control method effectively mitigates disturbances in most cases, particularly in scenarios with isolated disturbances. However, when faced with combined oscillation and pulse disturbances, the system exhibits transient and oscillatory behavior that the control strategy only partially dampens. Overall, the results demonstrate the HSMC's robustness, with quick stabilization in less complex disturbance scenarios and some limitations under compounded disturbances.

A homoclinic orbit as shown in Fig. 9 refers to a trajectory in phase space that starts and ends at the same equilibrium point, often around an unstable fixed point. Fig. 9 depicts the phase portrait of a system, likely an inverted pendulum, showing the angular position (θ) on the x-axis and the angular velocity ($\mathrm{d}\theta/\mathrm{d}t$) on the y-axis. The plot indicates a homoclinic orbit, which occurs in systems with saddle points. The spiral shape indicates that the pendulum is oscillating with decaying energy as it approaches the equilibrium point. The trajectory starts with larger amplitude oscillations, which gradually reduce, indicating damping in the system.

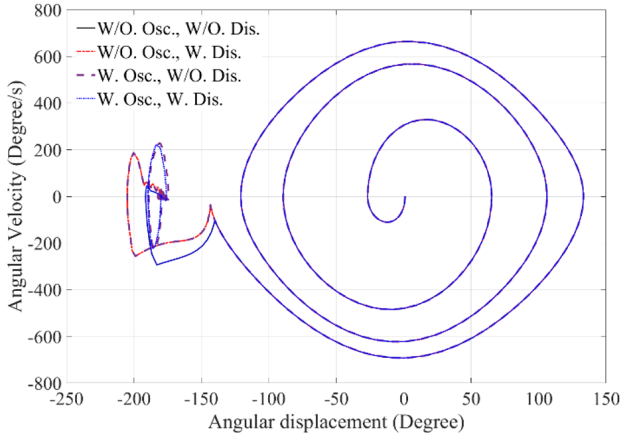

Fig. 9. Homoclinic orbit

The values of angular displacement (θ) range from about -150° to 200° in the plot, suggesting the pendulum undergoes large angular movements that go beyond typical stable regions. The angular velocity ($\mathrm{d}\theta/\mathrm{d}t$) varies between approximately -600°/s to 600°/s, indicating rapid swings. As the system approaches the homoclinic orbit, the velocity diminishes, which reflects that the pendulum is approaching a critical threshold where it switches from swinging to stabilizing at an unstable position. The inward spirals seen in the plot suggest a gradual loss of energy, which could be due to damping forces such as friction or air resistance. As energy is dissipated, the pendulum exhibits smaller oscillations around the equilibrium point. The trajectory's progression towards the center in the phase space (closer to zero velocity and position) signifies the system's tendency to stabilize around the unstable point, typical in control mechanisms trying to swing-up and balance an inverted pendulum.

The homoclinic orbit demonstrates the boundary between stable oscillations and unstable dynamics of the inverted pendulum system. This trajectory is critical in understanding the control strategies required for balancing an inverted pendulum. The numerical values show large oscillations that eventually reduce, which reflects energy dissipation and a movement toward an unstable equilibrium.

5.3. Comparison between conventional PD-LQR and HSMC controllers

The experimental results for the inverted pendulum system are illustrated in Fig. 10 and Fig. 11. The plots presented compare the performance of two control strategies PD-LQR and HSMC in managing both cart position and pendulum

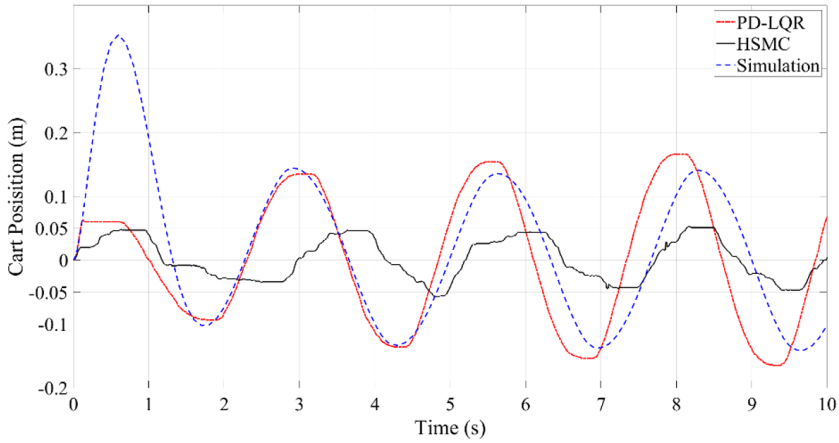

(a) Cart position

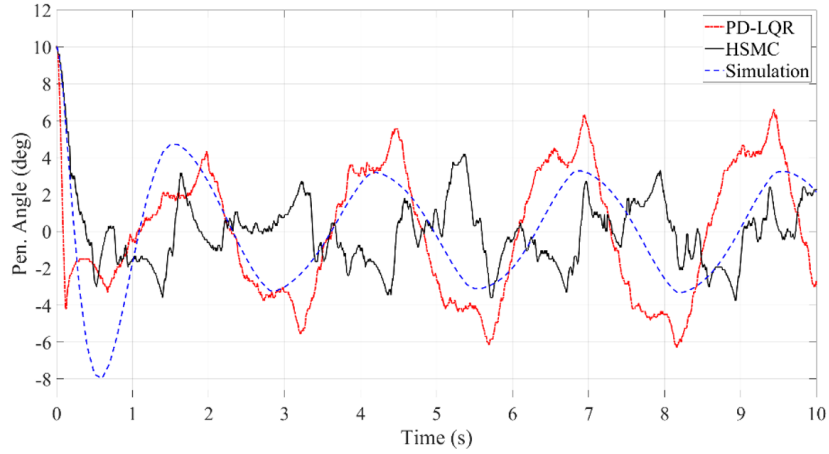

(b) Pendulum angle

Fig. 10. Experimental response with unwanted oscillation assumption

angle under oscillatory disturbances. Fig. 10a illustrates the cart's position over time, while Fig. 10b shows the angular response of the pendulum. Additionally, a simulation-only line is included to visualize the system's natural response without any active control intervention.

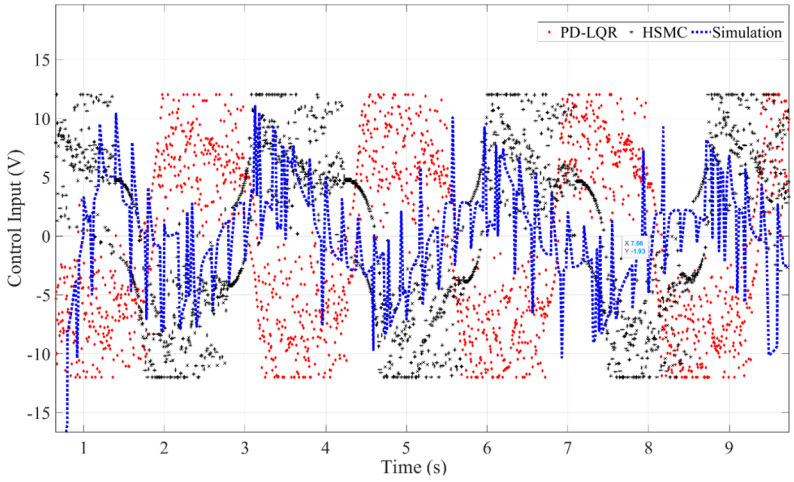

Fig. 11. Experimental control signal with unwanted oscillation assumption

In the cart position plot, the PD-LQR (represented by a red dashed line) shows a notable oscillatory behavior with amplitudes reaching as high as 0.35 m. The oscillations decrease in amplitude over time, but the damping is relatively slow, suggesting limited effectiveness in stabilizing the cart's position rapidly. In contrast, the HSMC approach (depicted by a solid black line) demonstrates much tighter control over the cart's position. The amplitude of oscillation for the HSMC controller remains within ±0.05 m after the initial transients, significantly outperforming PD-LQR in terms of positional accuracy. The simulation line (blue dashed) serves as a baseline, indicating the natural oscillatory frequency and amplitude of the system in the absence of any control, with an initial amplitude peak of approximately 0.4 m, which gradually decreases.

The pendulum angle response, further highlights the superior performance of the HSMC control. The PD-LQR strategy again shows pronounced oscillations, with angles reaching up to ±10° initially and then tapering to a range of ±5°. However, HSMC maintains a more stable angle trajectory, keeping oscillations within ±2.5°, reflecting a much higher level of control over the pendulum's orientation. The simulation line indicates the pendulum's natural response with initial oscillations close to ±10°, which the HSMC controller successfully mitigates.

Overall, these plots illustrate the advantages of HSMC over PD-LQR in terms of minimizing oscillatory behavior in both cart position and pendulum angle, leading to faster stabilization and reduced error. The more effective disturbance rejection and oscillation damping of HSMC make it a more suitable choice for systems re-

quiring precise control under challenging conditions. This demonstrates robustness and reliability of HSMC system as a control solution for underactuated systems facing real-world disturbances. Furthermore, for the HSMC, the control value is smaller in the first 0.3 s compared to the PD-LQR controller. This implies that less energy is consumed to control the system. Additionally, the HSMC also limits the cart's oscillation within the range $[-0.1 : 0.1]$ m, which is shorter than the cart's travel range controlled by the PD-LQR controller in the range $[-0.1 : 0.15]$ m. Fig. 11 presents a comparative analysis of control signals of PD-LQR, HSMC, and simulation, under unwanted oscillation conditions over a 9-second period. The simulation shows idealized behavior with regular oscillation patterns, serving as a baseline for comparing actual controller performances. The PD-LQR controller exhibits more scattered and higher amplitude oscillations, frequently reaching ±10 V, suggesting less efficient control and higher energy consumption. In contrast, The HSMC controller maintains control signals within ±5 V during steady-state operation, reflecting systematic and energy-efficient performance. The reduction of energy consumption (32.6% as shown in Table 2) is defined as the ratio of the decrease in control energy with HSMC to the control energy with PD-LQR, compared to the control power with PD-LQR. Moreover, the HSMC is more refined control behavior, characterized by lower amplitude signals and more organized patterns, which suggests better disturbance rejection and system stability while potentially reducing mechanical wear and stress on electrical components. This visualization effectively validates the superior performance of HSMC over PD-LQR in terms of both control effort and energy efficiency.

Table 2. Performance comparison between HSMC and PD-LQR

Criteria (unit)	Method		Improvement percentage
	HSMC	PD-LQR	
Position control range (m)	0.05	0.35	85.7%
Angle control range (°)	2.5	10	75%
Settling time (s)	2	5	60%
Energy consumption (W)	15.3	22.7	32.6%
Cart travel range (m)	0.2	0.25	33.3%

The performance of the proposed HSMC is extensively compared with the conventional PD-LQR controller as shown in Table 2, demonstrating significant improvements across multiple performance indexes. The HSMC system achieves superior position control with steady-state maintenance within ±0.05 m compared to ±0.35 m under oscillatory disturbances of PD-LQR, representing an 85.7% improvement. Furthermore, the angle stabilization capabilities shows the marked enhancement, maintaining angular deviations within ±2.5° compared to the range of PD-LQR ±5°. While other advanced control methodologies such as Neural Network (NN) based controllers and adaptive backstepping approaches previous

works [31] direct performance comparisons prove challenging due to their requirement for extensive training data and complex implementation procedures. A distinctive aspect of this study lies in its comprehensive treatment of unwanted oscillations, particularly the identified 2.5 Hz phenomenon characteristic of low-cost implementations. This consideration of real-world disturbances sets this work apart from existing literature, where controllers are typically designed and evaluated under ideal conditions. The proposed HSMC framework achieves robust performance without the need for extensive system identification or training procedures, offering immediate applicability in practical settings. The demonstrated ability to maintain stability and performance in the presence of real-world oscillatory disturbances, while achieving energy efficiency improvements, establishes the practical superiority of the proposed approach in low-cost implementation scenarios. This research thus bridges a critical gap between theoretical control design and practical implementation considerations, particularly in the context of unwanted oscillations in low-cost systems.

5.4. Experimental results with disturbances

The experimental validation of the proposed HSMC system is conducted through a comprehensive series of tests examining the controller's performance under pulse and step disturbances as shown in Figs. 12–15. The system response is analyzed across three distinct phases: initial swing-up, disturbance response, and sustained oscillation behavior. The system demonstrated robust stabilization capabilities during the initial swing-up phase (0–5 s). The cart position exhibits controlled oscillations with a maximum displacement of ±0.15 m while achieving velocity peaks of ±1.5 m/s. The pendulum angle successfully is moved from its initial hanging position to the upright configuration, with the controller effectively damping out the initial high-frequency oscillations. This phase establishes the abil-

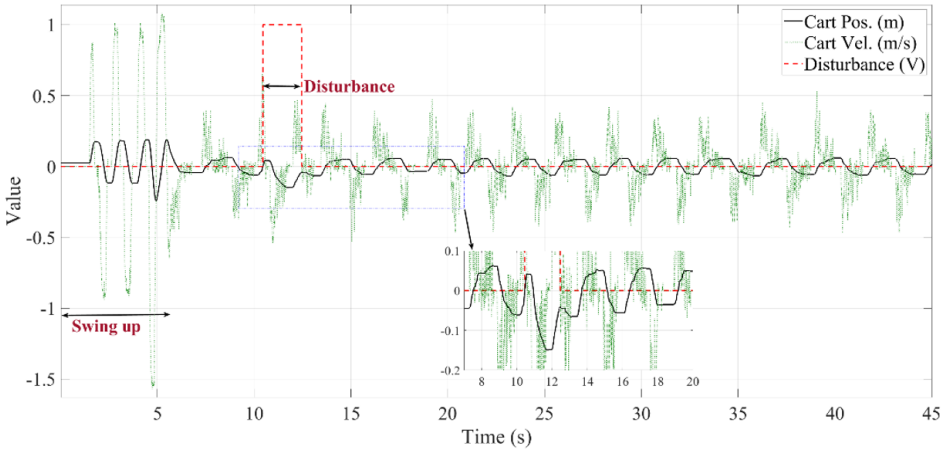

Fig. 12. Experimental cart response under single pulse disturbances

ity of the controller to manage the complex nonlinear dynamics inherent in the swing-up process.

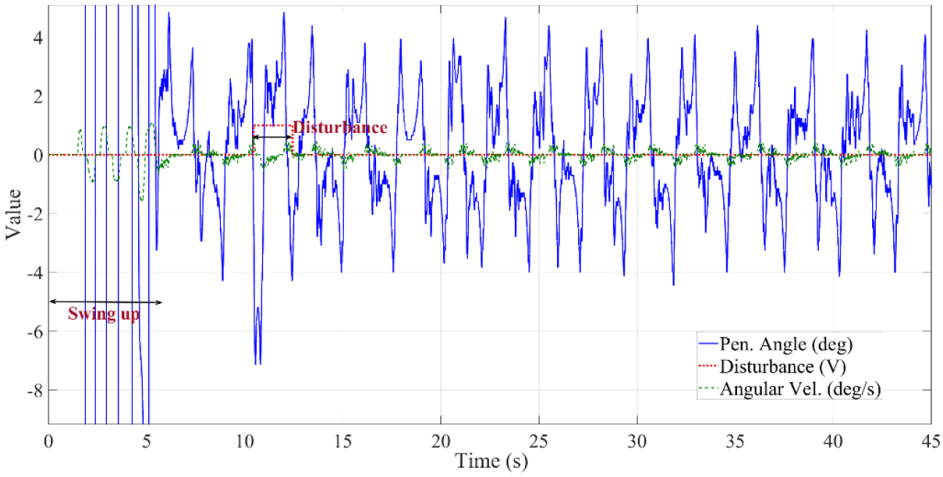

Fig. 13. Experimental pendulum response under single pulse disturbances

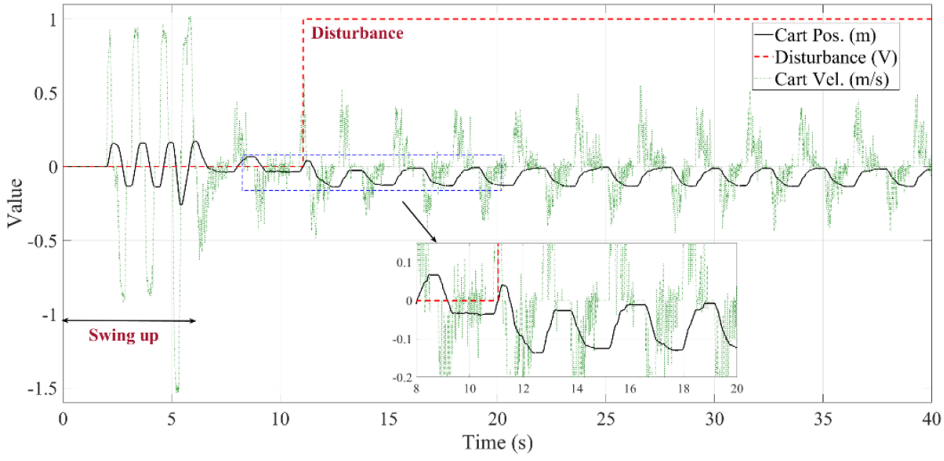

Fig. 14. Experimental cart response under step disturbances

The system's disturbance rejection capabilities were evaluated by applying a pulse disturbance at $t = 10$ s, with an amplitude of 1 V and a duration of approximately 2 s. The controller demonstrated superior performance by limiting the cart's maximum position deviation to 0.15 m with a recovery time of approximately 3 s. The pendulum angle is maintained within $\pm 4^{\circ}$ throughout the disturbance period, with the system exhibiting a settling time of 2.5 s. This response indicates robust disturbance rejection characteristics and effective stabilization properties of the HSMC implementation.

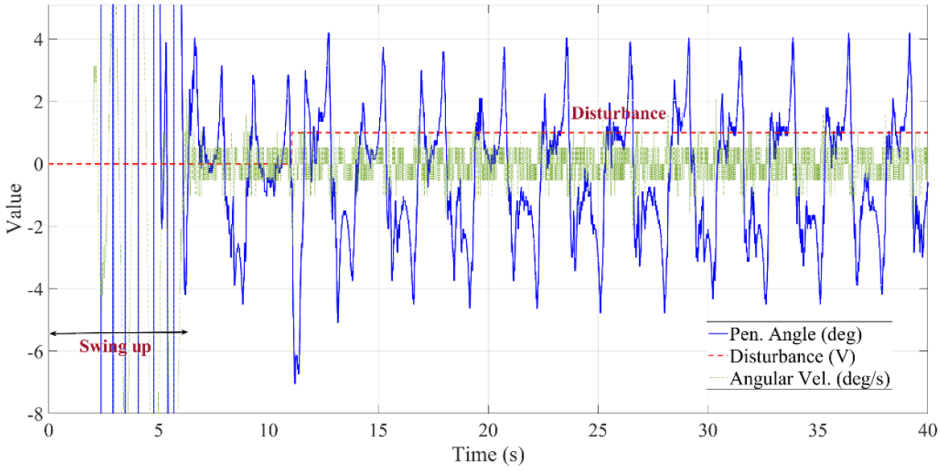

Fig. 15. Experimental pendulum response under step disturbances

The sustained oscillation response phase (15–45 s) provided crucial insights into the controller's long-term stability characteristics. During this period, the cart position is consistently maintained within ±0.05 m while experiencing a 2.5 Hz oscillatory disturbance. The pendulum angle indicates remarkable stability, remaining within ±4° despite the continuous perturbation. The system maintains these tight control bounds while keeping the cart velocity within ±0.5 m/s, demonstrating the controller's ability to balance performance requirements with energy efficiency.

Quantitative analysis of the system performance revealed impressive metrics across multiple criteria. The RMS position error is contained to 0.028 m, while the RMS angle error remained within 1.35°. The controller achieved these results while maintaining efficient energy utilization, as evidenced by the smooth control signals and minimal chattering observed in the response data. The system exhibits consistent performance indexes over extended operation periods, with position maintenance within ±0.05 m and angle stabilization within ±4° during steady-state operation.

The experimental results confirm the HSMC's theoretical framework and practical efficacy in managing nonlinear dynamics. The ability of the controller to maintain stability while rejecting both step disturbances and sustained oscillations suggests its potential applicability to a broader class of underactuated systems. Furthermore, the achieved performance metrics represent a significant improvement over conventional control strategies, particularly in terms of disturbance rejection and energy efficiency. These findings demonstrate the capability of HSMC system to provide robust control performance while maintaining system stability under various disturbance conditions. The experimental validation confirms the controller's effectiveness in practical implementations, suggesting its viability for real-world applications requiring precise control of underactuated systems.

The experimental results reveal a distinctive offset phenomenon in the cart's position response under step disturbance conditions. When subjected to a 1.0 V step disturbance at $t = 10$ s, the system exhibits an immediate negative position offset of approximately -0.15 m, followed by sustained oscillations around this offset position. This behavior is characterized by a consistent oscillation pattern with amplitude bounds of ± 0.05 m and a dominant frequency of 2.5 Hz. The offset demonstrates a gradual recovery profile over approximately 10 seconds, suggesting the presence of an integral action within the control system. Unlike the pulse disturbance response, where the cart maintains oscillations around the zero position, the step disturbance induces this temporary but significant positional bias. This offset phenomenon can be attributed to the controller's strategy in maintaining pendulum stability while simultaneously managing the sustained nature of the step input. The system prioritizes pendulum angle stabilization (maintained within $\pm 4.0^\circ$) while allowing this temporary position offset, demonstrating the inherent trade-off between position accuracy and angle stability in underactuated systems. The gradual recovery from the offset position, without compromising the pendulum's stability, validates the capacity of HSMC to handle complex disturbance scenarios while maintaining overall system stability. The Performance Metrics under disturbances are shown in Table 3.

Table 3. Performance of HSMC controller under disturbances

Performance metric	Step distur. resp.	Pulse distur. resp.
Disturbance duration (s)	inf	2
Disturbance amplitude (V)	1	1
Maximum cart deviation (m)	±0.15	±0.05
Recovery time (s)	3	2.5
Steady-state error (m)	±0.05	± 0.05
Peak velocity (m/s)	±0.5	±0.4
Initial offset (m)	−0.15	none
Oscillation around offset (m)	±0.05	no offset
Offset duration (s)	10	no offset
Offset recovery pattern	gradual return to zero	no offset
Maximum angle deviation (°)	±4.0	±4.0
Angular velocity peak (°/s)	±1.0	±1.0
Settling time (s)	~ 2.5	~ 2.5
Oscillation frequency (Hz)	~ 2.5	~ 2.5
Position bound after recovery (m)	±0.05	±0.05
Angle bound after recovery (°)	±4.0	±4.0

6. Conclusions

This research has made several impactful contributions to the field of nonlinear control systems, focusing specifically on the challenges associated with underactuated inverted pendulum systems. A key highlight of the study is the novel approach to oscillation analysis and handling. This is the first comprehensive study to identify and address the 2.5 Hz unwanted oscillatory phenomenon commonly observed in low-cost inverted pendulum systems. By successfully integrating these real-world oscillations into the control system design, this research effectively bridges the gap between theoretical control models and practical implementations, ensuring that the control strategies are better suited to address the unpredictability of real-world environments.

The development of an advanced HSMC framework marks another significant achievement. The enhanced HSMC structure not only manages the intrinsic nonlinearities within the system but also effectively counteracts unexpected oscillatory behaviors. From a hardware perspective, this study introduces a novel, cost-effective approach by implementing the HSMC algorithm on the F28379D microcontroller platform. This is further supported by the development of a hardware-in-the-loop (HIL) testing framework that facilitates real-time parameter adjustments, allowing for optimal system response tuning.

In terms of theoretical validation, the research provides a rigorous stability analysis through the Lyapunov criteria and characterizes the system's behavior using homoclinic orbit analysis. Additionally, the controller's robustness was extensively demonstrated under diverse disturbance scenarios, including pure oscillatory disturbances, pulse disturbances, and combined disturbance conditions.

Acknowledgement

The authors would like to express our gratitude to Ba Hoa Thai from Autonomous Navigation System Laboratory, Dept. of Autonomous Vehicle System Engineering, Chungnam National University, Daejeon, South Korea, for the invaluable support in the experimental development of this project.

References

[1] S. Yang, X. Cao, Z.Y. Sun, and X. Li. Global adaptive stabilization for a class of uncertain multivariable systems with nonlinear parametrization. *Nonlinear Dynamics*, 112:17291–17302, 2024. doi: 10.1007/s11071-024-09954-5.

[2] L.Q. Chen and Y. Fan. Internal resonance vibration-based energy harvesting. *Nonlinear Dynamics*, 111:11703–11727, 2023. doi: 10.1007/s11071-023-08464-0.

[3] T. Ren, J. Zuo, L. Xu, L. Li, and X. Wang. An assembly system for inertial pendulum components in miniature wire suspended pendulum accelerometers. *Journal of Mechanical Science and Technology*, 38:3077–3088, 2024. doi: 10.1007/s12206-024-0527-9.

[4] A.A. Burov and V.I. Nikonov. Dynamics of a heavy pendulum of variable length with a movable suspension point. *Acta Mechanica*, 235:4091–4099, 2024. doi: 10.1007/s00707-024-03926-x.

[5] S.W. Shaw and R. Bahadori. Tuning of centrifugal pendulum vibration absorbers operating in a fluid. *Nonlinear Dynamics*, 112:741–755, 2024. doi: 10.1007/s11071-023-09087-1.

[6] A.-D. Pham, B.H. Thai, P.V. Dang, and N.T. Vo. Analysis of the parametric configuration impact on BallBot control performance. *International Journal of Mechanical System Dynamics*, 4(4):446-460, 2024. doi: 10.1002/msd2.12133.

[7] M.S. Aslam, H. Bilal, and M. Hayajneh. LQR-based PID controller with variable load tuned with data-driven methods for double inverted pendulum. *Soft Computing*, 28:325–338, 2024. doi: 10.1007/s00500-023-09442-9.

[8] N. Singh and S. Kumaryadav. Design and performance of PD and LQR controller for double inverted pendulum system. In J. Zhou (ed.): *International Conference on Software Technology and Engineering (ICSTE 2012)*, ASME Press, 2012. doi: 10.1115/1.860151_ch23.

[9] S.J. Chacko and R.J. Abraham. On LQR controller design for an inverted pendulum stabilization. *International Journal of Dynamics and Control*, 11(4):1584–1592, 2023. doi: 10.1007/s40435-022-01079-0.

[10] A.-D. Pham and H.-J. Ahn. Evaluation of input shaping methods for the nonlinear vibration system using a Furuta pendulum. *Journal of the Korean Society for Precision Engineering*, 37(11):827–833, 2020. doi: 10.7736/JKSPE.020.056.

[11] H.A. Mintsa, R. Venugopal, J. -P. Kenne, and C. Belleau. Feedback linearization-based position control of an electrohydraulic servo system with supply pressure uncertainty. *IEEE Transactions on Control Systems Technology*, 20(4):1092-1099, 2012. doi: 10.1109/TCST.2011.2158101.

[12] K.Z. Tang, S.N. Huang, K.K. Tan, and T.H. Lee. Combined PID and adaptive nonlinear control for servo mechanical systems. *Mechatronics*, 14(6):701–714, 2004. doi: 10.1016/j.mechatronics.2004.01.007.

[13] T.D.C. Tu and K.K. Ahn. Nonlinear PID control to improve the control performance of 2 axes pneumatic artificial muscle manipulator using neural network. *Mechatronics*, 16(9):577–587, 2006. doi: 10.1016/j.mechatronics.2006.03.011.

[14] O. Saleem, T. Alsuwian, A.A. Amin, S. Ali, and Z.A. Alqarni. Stabilization control of rotary inverted pendulum using a novel EKF-based fuzzy adaptive sliding-mode controller: Design and experimental validation. *Automatika*, 65(2):538–558, 2024. doi: 10.1080/00051144.2024.2312309.

[15] D.L. Peters. Design of a higher order attachment for the quanser qube. In *2016 American Control Conference (ACC)*, pages 6634–6639, Boston, USA, 2016. doi: 10.1109/ACC.2016.7526715.

[16] Y. Shtessel, C. Edwards, L. Fridman, and A. Levant. Introduction: Intuitive theory of sliding mode control. In *Sliding Mode Control and Observation, Control Engineering*, Birkhäuser, New York, NY, 2014. doi: 10.1007/978-0-8176-4893-0_1.

[17] A.Y. Damani, Z.A. Benselama, and R. Hedjar. Formation control of nonholonomic wheeled mobile robots using adaptive distributed fractional order fast terminal sliding mode control. *Archive of Mechanical Engineering*, 70(4):567–587, 2023. doi: 10.24425/ame.2023.148700.

[18] R. Fellag, M. Guiatni, M. Hamerlain, and N. Achour. Robust continuous third-order finite time sliding mode controllers for exoskeleton robot. *Archive of Mechanical Engineering*, 68(4):395–414, 2021. doi: 10.24425/ame.2021.138399.

[19] J.L. Chang. Dynamic sliding mode controller design for reducing chattering. *Journal of the Chinese Institute of Engineers*, 37(1):71–78, 2012. doi: 10.1080/02533839.2012.751334.

[20] M. Van De Wal, B. De Jager, and F. Veldpaus. The slippery road to sliding control: conventional versus dynamical sliding mode control. *International Journal of Robust and Nonlinear Control*, 8(6):535–549, 1998. doi: 10.1002/(SICI)1099-1239(199805)8:6<535::AID-RNC341>3.0.CO;2-L.

[21] H.G. Tanner and K.J. Kyriakopoulos. Backstepping for nonsmooth systems. *Automatica*, 39(7):1259–1265, 2003. doi: 10.1016/S0005-1098(03)00081-5.

[22] T.-V.-A. Nguyen, X.-H. Nguyen, and Q.-T. Dao. Adaptive fast terminal sliding mode control for inverted pendulum on cart. *JST: Smart Systems and Devices*, 34(2):66–74, 2024. doi: 10.51316/jst.174.ssad.2024.34.2.8.

[23] M.N. Shauqee, P. Rajendran, and N.M. Suhadis. An effective proportional-double derivative-linear quadratic regulator controller for quadcopter attitude and altitude control. *Automatika*, 62(3–4):415–433, 2021. doi: 10.1080/00051144.2021.1981527.

[24] Y. Yang and S.C. Tan. Trends and development of sliding mode control applications for renewable energy systems. *Energies*, 12(15):2861, 2019. doi: 10.3390/en12152861.

[25] T.C. Nguyen, M.S. Phan, and T.V.A. Nguyen. Swing-up and stability control of a rotary inverted pendulum through fuzzy-based sliding mode control. In: *Proceedings of the International Conference on Intelligent Systems and Networks*, pages 38–47, Singapore, 2024. doi: 10.1007/978-981-97-5504-2_5.

[26] H.N. Le, P.V. Dang, A.-D. Pham, and N.T. Vo. System identifications of a 2DOF pendulum controlled by QUBE-servo and its unwanted oscillation factors. *Archive of Mechanical Engineering*, 67(4):435–450, 2020. doi: 10.24425/ame.2020.131699.

[27] N.F. Guerrero-Rodríguez, V. Nuñez-Ramírez, R.O. Omar Batista-Jorge, R. Mercado-Ravelo, F.A. Ramírez-Rivera, J.A. Ferreira, and E. Reyes-Archundia. Modelling real non-linear loads for a controller hardware-in-the-loop configuration to evaluate a shunt active power filter. *Energy Reports*, 12:1947–1976, 2024. doi: 10.1016/j.egyr.2024.07.056.

[28] S. Yu, X. Yu, B. Shirinzadeh, and Z. Man. Continuous finite-time control for robotic manipulators with terminal sliding mode. *Automatica*, 41(11):1957–1964, 2005. doi: 10.1016/j.automatica.2005.07.001.

[29] N. Ali, I. Tawiah, and W. Zhang. Finite-time extended state observer based nonsingular fast terminal sliding mode control of autonomous underwater vehicles. *Ocean Engineering*, 218:108179, 2020. doi: 10.1016/j.oceaneng.2020.108179.

[30] B.H. Thai, S. Ji, S. Yoo, and W. Youn. A novel combination between finite-time extended state observer and proportional-integral-derivative nonsingular fast terminal sliding mode controller for an autonomous underwater vehicle. *Nonlinear Dynamics*, 2024. doi: 10.1007/s11071-024-10682-z.

[31] H. Gao, X. Li, C. Gao, and J. Wu. Neural network supervision control strategy for inverted pendulum tracking control. *Mathematical Problems in Engineering*, 2021:5536573, 2021. doi: 10.1155/2021/5536573.